

No *Catch-22* for Fuzzy Dark Matter: testing substructure counts and core sizes via high-resolution cosmological simulations

Sana Elgamal^{1,2*}, Matteo Nori^{1,2}, Andrea V. Macciò^{1,2,3}, Marco Baldi^{4,5,6},
Stefan Waterval^{1,2}

¹New York University Abu Dhabi, PO Box 129188 Saadiyat Island, Abu Dhabi, United Arab Emirates

²Center for Astrophysics and Space Science (CASS), New York University Abu Dhabi, PO Box 129188, Abu Dhabi, UAE

³Max Planck Institut für Astronomie, Königstuhl 17, D-69117 Heidelberg, Germany

⁴Dipartimento di Fisica e Astronomia, Alma Mater Studiorum - University of Bologna, Via Piero Gobetti 93/2, 40129 Bologna BO, Italy

⁵INAF - Osservatorio Astronomico di Bologna, Via Piero Gobetti 93/3, 40129 Bologna BO, Italy

⁶INFN - Istituto Nazionale di Fisica Nucleare, Sezione di Bologna, Viale Berti Pichat 6/2, 40127 Bologna BO, Italy

Accepted XXX. Received YYY; in original form ZZZ

ABSTRACT

Fuzzy Dark Matter (FDM) has recently emerged as an interesting alternative model to the standard Cold Dark Matter (CDM). In this model, dark matter consists of very light bosonic particles with quantum mechanical effects on galactic scales. Using the N -body code AX-GADGET, we perform cosmological simulations of FDM that fully model the dynamical effects of the quantum potential throughout cosmic evolution. Through the combined analysis of FDM volume and high-resolution zoom-in simulations of different FDM particle masses ($m_\chi \sim 10^{-23} - 10^{-21}$ eV/ c^2), we study how FDM impacts the abundance of substructure and the inner density profiles of dark matter haloes. For the first time, using our FDM volume simulations, we provide a fitting formula for the FDM-to-CDM subhalo abundance ratio as a function of the FDM mass.

More importantly, our simulations clearly demonstrate that there exists an extended FDM particle mass interval able to reproduce the observed substructure counts and, at the same time, create substantial cores ($r_c \sim 1$ kpc) in the density profile of dwarf galaxies ($\approx 10^9 - 10^{10}$ M_\odot), which stands in stark contrast with CDM predictions even with baryonic effects taken into account. The dark matter distribution in the faintest galaxies offers then a clear way to discriminate between FDM and CDM.

Key words: cosmology: theory – methods: numerical

1 INTRODUCTION

Evidence for dark matter has accumulated from an array of observations spanning a wide range of scales. On galactic scales, the observed rotation curves of galaxies remain relatively flat at large radii, which significantly deviates from the theoretical expectation derived solely from the visible matter (Rubin et al. 1980; Bosma 1981). On cluster scales, the mass-to-light ratios of galaxy clusters are significantly larger than unity (Zwicky 1937; Bahcall et al. 1995), providing evidence for the presence of a massive non-luminous component. Moving on to cosmological scales, observations of the large-scale structure (Tegmark et al. 2006) require

the existence of a non-relativistic clustering component that decoupled from the hot primordial plasma well before recombination in order to explain the highly non-linear structure that we observe in the Universe today. In addition, the observed Cosmic Microwave Background (CMB) anisotropies (Komatsu et al. 2011; Planck Collaboration et al. 2016) along with observations from Type IA Supernovae (Riess et al. 1998; Perlmutter et al. 1999) constrain the total matter energy density in the Universe, which has been found to greatly exceed the baryon density from Big Bang Nucleosynthesis (Copi et al. 1995). This provides further evidence for the existence of an additional gravitational component of non-baryonic origin. Taken together, these independent observations have built a compelling case for the presence

* E-mail: selgamal@uchicago.edu

of a non-luminous, non-baryonic, clustering component that dominates the matter content of the Universe.

The current picture of cosmological structure formation heavily relies on the existence of the so-called Cold Dark Matter (CDM), whose physical nature remains unknown. While the standard hierarchical CDM picture has proven to provide a remarkably successful description of large-scale cosmological observations (Tegmark et al. 2006; Aghanim et al. 2020; Alam et al. 2017), assessing its validity on highly nonlinear scales has proven to be a much more challenging task. On the theoretical front, baryonic physics is known to play a significant role on those scales (Brooks & Zolotov 2014; Oñorbe et al. 2015; Macciò et al. 2020; Waterval et al. 2022), with effects that are difficult to disentangle from those arising from the fundamental nature of dark matter. On the observational side, the inefficiency of star formation particularly in dwarf galaxies (Yang et al. 2003; Fitts et al. 2017; Frings et al. 2017) renders their detection difficult, making it harder to perform a robust measurement of the subhalo mass function of the Local Group. This, combined with the lack of direct detection of the dark matter particles in the $\mathcal{O}(\text{GeV}/c^2)$ mass scale has motivated efforts to formulate and explore models beyond the standard CDM paradigm. Since the success of CDM is extremely well-established on linear scales, it follows that any alternative model of dark matter needs to match the behaviour of CDM on large scales in order to constitute a viable model of structure formation.

One such particle dark matter alternative is Fuzzy Dark Matter (FDM), which – with motivations from particle theory – posits that dark matter consists of extremely light bosons (Hu et al. 2000). The bosons possess a very small mass which Hu et al. (2000) originally proposed to be $\mathcal{O}(10^{-22} \text{ eV}/c^2)$ (see also Amendola & Barbieri 2006, for the first limits on FDM). This extremely low mass corresponds to a de Broglie wavelength on scales of $\mathcal{O}(1 \text{ kpc})$, meaning that the wave-like behaviour of FDM manifests on those sub-galactic scales (see e.g. Hui et al. 2017a; Ferreira 2021, for comprehensive reviews).

The quantum nature of FDM is encapsulated in a potential form referred to as “quantum potential” which arises due to the uncertainty principle. This quantum potential counteracts gravity and hence stabilizes the small-scale density perturbations against collapse. Therefore, unlike CDM, where the density perturbations are unstable and thus able to collapse on all spatial scales below the Hubble horizon, the quantum potential in FDM introduces a characteristic scale below which perturbations are stable. This gives rise to a suppression of the formation of low-mass haloes and subhaloes, which effectively translates to a sharp reduction in the FDM linear power on small scales. In addition to this, the quantum potential also impacts the internal structure of FDM subhaloes. In fact, FDM subhaloes naturally have cored (i.e., flat) instead of cuspy (i.e., with density diverging as $\propto 1/r$) inner density profiles, since the quantum potential limits the central density of collapsed subhaloes (Hui et al. 2017a).

The mass of the FDM particle – denoted hereafter as m_χ – is the only free parameter in the FDM model. To ensure that the field behaves like dark matter while remaining relevant in cosmological structure formation and reionization, the mass of the FDM particle should fall within the

range $10^{-33} \text{ eV}/c^2 \lesssim m_\chi \lesssim 10^{-18} \text{ eV}/c^2$. On linear scales, observational signatures constrain the FDM particle mass to $m_\chi \gtrsim 10^{-24} \text{ eV}/c^2$ (Marsh 2016b). Since the quantum potential term only dominates below scales comparable to the de Broglie scale, deriving useful constraints on m_χ requires investigation of the non-linear scales. While those scales in principle possess rich cosmological information that can be utilised to further constrain the FDM mass, they are nonetheless complicated by effects arising from baryonic physics which are still only partially understood. Despite this uncertainty, efforts are under way to establish constraints on m_χ from the non-linear scales. Amorisco & Loeb (2018) used stellar streams to constrain the FDM particle mass to be $m_{22} \gtrsim 1.5$ (hereafter $m_{22} \equiv m_\chi/10^{-22} \text{ eV}/c^2$). Furthermore, since the quantum potential delays the onset of structure formation and hence galaxy formation in FDM, Kulkarni & Ostriker (2022) utilized observations of high-redshift lensed galaxies to impose a constraint of $m_{22} \gtrsim 2$ on the FDM mass.

Additionally, observations of the Lyman- α forest trace the dark matter distribution in the high-redshift Universe, allowing the inference of the matter power spectrum on scales $0.3 h \text{ Mpc}^{-1} \lesssim k \lesssim 12.5 h \text{ Mpc}^{-1}$ and thus providing a robust means of testing and constraining the nature of dark matter. Accounting for the full non-linear treatment of the quantum potential, measurements of the 1D Lyman- α forest flux power spectrum yielded a lower bound of $\approx 21.08 \times 10^{-22} \text{ eV}/c^2$ on the FDM mass at the 2σ level (Nori et al. 2019).

In a variant to CDM (that is often considered to be akin to FDM) known as Warm Dark Matter (WDM), dark matter consists of standard collisionless particles whose mass is sufficiently small $\sim \mathcal{O}(1 \text{ keV}/c^2)$ that its primordial velocity dispersion significantly impacts structure formation through free-streaming, suppressing the formation of substructure and inducing core formation in dwarf galaxies (Viel et al. 2005; Abazajian 2006; Lovell et al. 2014b).

However, Macciò et al. (2012) demonstrated the presence of a *Catch-22* problem within the framework of a WDM universe. This refers to the absence of a WDM particle mass interval that can account for the observed abundance of substructures and the substantial density cores inside dwarf galaxies *simultaneously*. In fact, in order to form the observed significant core ($\sim 1 \text{ kpc}$) inside a dwarf galaxy, a thermal candidate mass of $\sim 0.1 \text{ keV}/c^2$ is required. This mass already prevents the formation of the galaxy through free-streaming. On the other hand, to form the dwarf galaxy itself, a candidate mass range of $\sim 1 - 2 \text{ keV}/c^2$ is needed, but this range fails to produce the observed large cores.

Using numerical simulations of structure formation that incorporate the characteristic non-linear interaction of FDM dynamics, and by computing the substructure abundance and inner density profiles of subhaloes for different FDM particle masses, the goal of this work is to test whether a similar *Catch-22* problem exists in an FDM universe.

The rest of this paper is structured as follows. In Sec. 2 we review the theoretical background of FDM cosmology. In Sec. 3 we detail our numerical methodology. In Sec. 4 we present our FDM Halo Mass Function and SubHalo Mass Function (hereafter HMF and SHMF, respectively) as measured from our cosmological volume simulations. We also

present the FDM radial density profiles which are derived from our zoom-in simulations. We then use observations of the SHMF and density profiles of dwarf galaxies surrounding the Milky Way in conjunction with our results to assess whether there is a *Catch-22* problem in FDM. A summary of our findings and conclusions is provided in Sec. 5. Additionally, we present the FDM concentration-mass relation computed using our volume simulations in Appendix A.

2 THEORY

The action of the scalar field ϕ describing FDM takes the following form:

$$S = \int \frac{d^4x}{\hbar c^2} \sqrt{-g} \left\{ \frac{1}{2} g^{\mu\nu} \nabla_\mu \phi \nabla_\nu \phi - \frac{1}{2} \frac{m_\chi^2 c^2}{\hbar^2} \phi^2 \right\}, \quad (1)$$

where $g^{\mu\nu}$ is the metric tensor for the perturbed Friedmann-Lemaître-Robertson-Walker (FLRW) metric given by:

$$ds^2 = \left(1 + \frac{2\Phi}{c^2} \right) c^2 dt^2 - a^2(t) \left(1 - \frac{2\Phi}{c^2} \right) d\mathbf{r}^2, \quad (2)$$

where $\Phi(\mathbf{r}, t)$ denotes the Newtonian gravitational potential and $a(t)$ is the scale factor. In the non-relativistic limit (which is relevant in the context of structure formation), it is convenient to express the real field ϕ in terms of another complex scalar field ψ :

$$\phi = \sqrt{\frac{\hbar^3 c}{2m_\chi}} \left(\psi e^{-im_\chi c^2 t/\hbar} + \psi^* e^{im_\chi c^2 t/\hbar} \right). \quad (3)$$

Using the non-relativistic assumption that ψ is slowly changing with time $|\dot{\psi}| \ll \frac{m_\chi}{\hbar} c^2 |\psi|$ (where dots denote cosmic time derivatives), one obtains the following equation of motion:

$$i\hbar \left(\dot{\psi} + \frac{3}{2} H \psi \right) = \left(-\frac{\hbar^2}{2m_\chi a^2} \nabla^2 + m_\chi \Phi \right) \psi, \quad (4)$$

which takes the form of the Schrödinger equation in an expanding universe. Here $H(t) \equiv \frac{\dot{a}}{a}$ is the Hubble parameter.

When studying cosmological structure formation, it is often useful to adopt the fluid approach. By performing a Madelung transformation (Madelung 1927), the equations can be reformulated from a field description to a fluid description. We define the dark matter fluid density ρ and velocity \mathbf{v} by:

$$\rho \equiv m|\psi|^2, \quad \mathbf{v} \equiv \frac{\hbar}{am} \nabla \theta = \frac{-i\hbar}{2ma} \left(\frac{\nabla \psi}{\psi} - \frac{\nabla \psi^*}{\psi^*} \right), \quad (5)$$

where θ represents the phase in $\psi = \sqrt{\frac{\rho}{m}} e^{i\theta}$. One can then recast the Schrödinger equation (Eq. 4) into the following fluid equations (Eqs. 6 and 7) in comoving coordinates:

$$\dot{\rho} + 3H\rho + \frac{1}{a} \nabla \cdot (\rho \mathbf{v}) = 0, \quad (6)$$

$$\dot{\mathbf{v}} + H\mathbf{v} + \frac{1}{a} (\mathbf{v} \cdot \nabla) \mathbf{v} = -\frac{1}{a} \nabla \Phi + \frac{\hbar^2}{2a^3 m_\chi^2} \nabla \left(\frac{\nabla^2 \sqrt{\rho}}{\sqrt{\rho}} \right), \quad (7)$$

by equating the imaginary and real parts of Eq. 4, respectively. Eq. 6 is the continuity equation while Eq. 7 resembles

an Euler equation with an additional quantum potential Q term defined by:

$$Q \equiv \frac{\hbar^2}{2m_\chi^2} \left(\frac{\nabla^2 \sqrt{\rho}}{\sqrt{\rho}} \right) = \frac{\hbar^2}{4m_\chi^2} \left(\frac{\nabla^2 \rho}{\rho} - \frac{|\nabla \rho|^2}{2\rho^2} \right). \quad (8)$$

To describe the behavior of the gravitational potential in response to fluctuations in the dark matter density field, Eqs. 6 and 7 need to be coupled to the Poisson equation:

$$\nabla^2 \Phi = 4\pi G a^2 \bar{\rho} \delta, \quad (9)$$

where $\delta \equiv \frac{\rho - \bar{\rho}}{\bar{\rho}}$ denotes the density contrast relative to the background density $\bar{\rho}$. Together with Eqs. 6 and 7, they comprise the Schrödinger-Poisson system. Perturbing Eqs. 6 and 7 around $\rho = \bar{\rho}$, $|\mathbf{v}| = 0$, and $\Phi = 0$, the density contrast in Fourier space – denoted as δ_k – satisfies the following equation (in the comoving frame) for a harmonic oscillator with a time-dependent mass term due to both gravity and the quantum potential as well as a friction term due to the Hubble expansion:

$$\ddot{\delta}_k + 2H\dot{\delta}_k + \left(\frac{\hbar^2 k^4}{4m_\chi^2 a^4} - \frac{4\pi G \rho_0}{a^3} \right) \delta_k = 0, \quad (10)$$

where k is the comoving wavenumber and $\rho_0 = \bar{\rho} a^3$ is the comoving FDM background density. From the negative sign in the mass term in Eq. 10, one observes that in addition to the usual gravitational term which reinforces the growth of FDM perturbations, the extra term due to the quantum potential counteracts such growth. Evidently, the FDM perturbations grow if gravity wins over the quantum potential $\left(\frac{\hbar^2 k^4}{4m_\chi^2 a^4} < \frac{4\pi G \rho_0}{a^3} \right)$. One can then readily identify the characteristic scale – referred to as the quantum Jeans scale – at which the gravitational attraction exactly balances the repulsion due to the quantum potential:

$$k_J = \left(\frac{16\pi G \rho_0 m_\chi^2}{\hbar^2} \right)^{1/4} a^{1/4}. \quad (11)$$

This means that the quantum potential in FDM introduces a threshold radius below which perturbations are unable to collapse. A corresponding quantum Jeans mass is then defined as the mass enclosed within the comoving radius $r = \frac{\pi}{k_J}$:

$$M_J = \frac{4\pi}{3} \rho_0 \left(\frac{\pi}{k_J} \right)^3 \propto a^{-3/4} m_\chi^{-3/2}, \quad (12)$$

and it represents the characteristic mass scale below which gravitational collapse and hence structure formation is prevented by FDM interaction at a particular redshift.

To find the growing solution for Eq. 10, we factorize δ_k into a factor that depends only on k and another time-dependent factor $D(t)$ by writing $\delta_k = A_k D(t)$. Plugging this in Eq. 10 gives the growing mode solution:

$$D_+(t) \propto \begin{cases} a, & k \ll k_J \\ 1, & k \gg k_J \end{cases}. \quad (13)$$

From Eq. 13, it can be inferred that structure formation in FDM is identical to that in CDM (where $D_+(t) \propto a$ for all k modes) on large scales ($k \ll k_J$), but – as already discussed – is suppressed on small scales ($k \gg k_J$). This implies that the linear power spectrum of FDM is expected

to match CDM on large scales. Indeed, it has been demonstrated using numerical simulations of structure formation that the large-scale structure of FDM is indistinguishable from that of CDM (Schive et al. 2014a).

In contrast to linear perturbation theory, where the growth of small-scale FDM density perturbations is evidently unable to catch up with that of the large-scale perturbations, non-linear theory predicts an enhanced growth of those small-scale perturbations. This enhancement arises from the interference between different k modes, which becomes particularly evident in the non-linear regime. As a consequence, density perturbations of order unity emerge on the de Broglie scale (Hui 2021). Indeed, cosmological simulations of FDM have demonstrated that perturbations on the quasi-linear and non-linear scales eventually catch up with the large-scale ones (at low redshifts), leading to a reduction in the amount of power suppression relative to CDM on those scales (Marsh 2016a; Nori & Baldi 2018).

2.1 Density cores

The Schrödinger-Poisson system (when solved along with the appropriate boundary conditions) can be shown to have a stable non-degenerate solution – i.e., the core – with different energy densities. The ground state solution is referred to as the “soliton” (Hui et al. 2017b; Chavanis 2011) and is characterized by the core density ρ_c and core radius r_c , which are defined as the finite density at $r = 0$ and the radius at which the density drops by one-half its value at $r = 0$ (i.e., $\rho(r_c) \equiv \rho_c/2$), respectively.

This soliton solution is found in the innermost regions of FDM subhaloes, which exhibit a flat central core. This is in contrast to the standard CDM subhaloes, whose density profiles are reasonably well-fitted by the Navarro-Frenk-White (Navarro et al. 1996), hereafter NFW) profile given by:

$$\rho(r) = \rho_s \left(\frac{4r_s^3}{r(r+r_s)^2} \right), \quad (14)$$

where r_s and ρ_s denote the characteristic scale radius and density at which the logarithmic density slope is -2 , respectively. Evidently, in the limit where $r \ll r_s$, the logarithmic density slope approaches -1 , while it approaches -3 for $r \gg r_s$.

Since the FDM quantum potential ceases to dominate over distances larger than the quantum Jeans scale, the FDM subhaloes typically exhibit an NFW envelope as in CDM. Consequently, FDM subhaloes are accurately described by a cored-NFW density profile (Chan et al. 2022; Schive et al. 2014b), which is given by:

$$\rho(r) = \begin{cases} \rho_c \left[1 + (\sqrt[8]{2} - 1) \left(\frac{r}{r_c} \right)^2 \right]^{-8} & r < r_t \\ 4\rho_s \left(\frac{r}{r_s} \right)^{-1} \left(1 + \frac{r}{r_s} \right)^{-2} & r \geq r_t \end{cases}, \quad (15)$$

where r_t denotes the radius at which the cored density profile transitions to an NFW.

The Schrödinger-Poisson system has an important scaling symmetry, where the system is invariant under the transformation $\{\tau, x, \psi, \Phi\} \rightarrow \{\lambda^{-2}\tau, \lambda^{-1}x, \lambda^2\psi, \lambda^2\Phi\}$ for an arbitrary scale factor λ (Ji & Sin 1994). This corresponds to the

following transformation of the relevant physical quantities $\{r_c, \rho_c\} \rightarrow \{\lambda^{-1}r_c, \lambda^4\rho_c\}$, which then fixes the core-scaling relation between r_c and ρ_c as follows:

$$r_c \propto (m_\chi^2 \rho_c)^{-1/4}. \quad (16)$$

3 NUMERICAL METHODS

To simulate structure and substructure formation, we use the N -body code AX-GADGET which is based on a particle-oriented solution of the Schrödinger-Poisson system and incorporates the quantum effects of FDM throughout cosmic evolution (see Nori & Baldi 2018, for a detailed description of the code).

To study the structure and substructure of FDM, we employ two distinct types of simulations. We utilize a set of eight cosmological volume simulation boxes, consisting of one CDM and seven FDM boxes with particle masses $m_{22} \in \{0.25, 0.50, 1.00, 2.00, 4.00, 8.00, 16.0\}$ ¹. In addition, we use a set of sixteen zoom-in simulations, representing four different low-mass systems, and each run using three FDM particle masses $m_{22} \in \{8.00, 16.0, 32.0\}$ along with their CDM counterpart. The FDM component comprises the entirety of the dark matter content within our simulations.

Those two different simulation sets together enable us to simultaneously attain sufficient large-scale resolution to obtain accurate HMF and SHMF averaged over a statistically large sample, as well as high small-scale resolution to characterize the features of the innermost density cores. Our choice of the FDM mass range $m_{22} \in [0.25 - 32.0]$ is motivated by its relevance at the scales of interest to both the SHMF and the density profiles.

Our volume and zoom-in simulation sets adopt cosmological parameters consistent with Planck Collaboration et al. (2016): matter density $\Omega_m = 0.317$, dark energy density $\Omega_\Lambda = 0.683$, Hubble constant $H_0 = 67.3 \text{ km s}^{-1} \text{ Mpc}^{-1}$, primordial matter power spectrum slope $n_s = 0.96$ and linear matter power spectrum normalization $\sigma_8 = 0.829$.

In order to ensure that the volume simulations represent the same volume of the Universe, all of the volume simulations in this work share the same seed for the random generation of the density perturbations. The specific distribution of perturbations is picked in accordance to the density power spectrum, which differs for CDM and each of the FDM models. We use the code axionCAMB (Hlozek et al. 2015) to compute the power spectra in the FDM scenario. The volume simulation boxes are cubical in shape with a co-moving side length of $20 h^{-1} \text{ Mpc}$, featuring 512^3 particles with a softening length of $300 h^{-1} \text{ pc}$ and a particle mass of $5.24 \cdot 10^6 h^{-1} M_\odot$.

¹ Note that, to preserve the symmetry of AX-GADGET internal units and their dependence on $h = H_0/100 \text{ km s}^{-1} \text{ Mpc}^{-1}$, the conversion to the physical FDM particle mass is $m_\chi = h^{-1/2} m_{22} 10^{-22} \text{ eV}/c^2$.

3.1 Halo identification, merger tree construction and fragmentation correction

The identification of collapsed objects and construction of the merger tree were performed employing the same methods as in [Springel et al. \(2008a\)](#), based on the SUBFIND code. The SUBFIND code uses a Friends-of-friends algorithm ([Davis et al. 1985](#)) to identify halo systems, which are then subdivided and disentangled into subhaloes based on binding energy considerations. In our analysis, we only include subhaloes that have a minimum of 128 particles. In the remainder of this text, we will refer to the overall dark matter system centered in the potential minimum as the halo, while the substructures within the halo are referred to as the satellites.

It is well-known that N -body simulations with suppressed initial power spectrum at small scales suffer from the so-called “numerical fragmentation” problem ([Wang & White 2007](#)). This refers to the formation of small collapsed objects due to numerical artifacts rather than the gravitational evolution of primordial overdensities.

To mitigate such contamination from spurious subhaloes, we utilize the same strategy used in [Nori et al. \(2019\)](#) (based in turn on [Wang & White 2007](#); [Lovell et al. 2014a](#)) which imposes cutoffs on the number of particles, mass and shape of FDM subhaloes. The remaining sample can then be reliably attributed to the evolution of overdensities.

The cutoff for the number of particles is set to 1000. For the mass cutoff scale estimate – denoted as M_{CUT} – we take into account the wavenumber at which the dimensionless power spectrum exhibits the highest amplitude k_{peak} along with the inter-particle distance d ([Lovell et al. 2014a](#); [Wang & White 2007](#)):

$$M_{\text{CUT}} \sim 5 \bar{\rho} \frac{d}{k_{\text{peak}}^2}. \quad (17)$$

Since we have FDM simulations with different particle masses (and hence different k_{peak} values), this scale cut-off will accordingly vary depending on the masses. Above this mass scale, the majority of the haloes can be safely considered to have a physical origin. As for the shape cut-off, we trace the halo particles back to their original positions in the initial conditions and use the sphericity s of their initial spatial distribution (i.e. the ratio of the minor and major semi-axes) as our constraint, which is obtained from the inertia tensor of the equivalent triaxial ellipsoid. We apply the sphericity threshold value $s_{\text{CUT}} = 0.16$ as determined by [Lovell et al. \(2014a\)](#) in the initial condition, below which the haloes are considered spurious. This value has also been verified to be valid in the FDM framework ([Nori et al. 2019](#)). Table 1 reports the M_{CUT} values used, as well as the total number of haloes (i.e., including those originating from numerical fragmentation) and genuine haloes in the FDM simulations with different masses. For general reference – even though CDM is not affected by numerical fragmentation –, we report that the number of haloes satisfying the number of particles and sphericity cutoff in CDM is 4205.

Model	N_{haloes}	N_{haloes} genuine	M_{CUT} [$10^{10} h^{-1} M_{\odot}$]
FDM-0.25	1803	226	1.00
FDM-0.50	2123	481	0.550
FDM-1.00	2375	903	0.300
FDM-2.00	3243	1635	0.165
FDM-4.00	5481	2474	0.0886
FDM-8.00	9727	3077	0.0481
FDM-16.0	15047	3309	0.0262
FDM-32.0	19310	3351	0.0142

Table 1. The total number of haloes, genuine haloes, and the mass cutoff for all the FDM simulations with different masses.

4 RESULTS

4.1 Halo Mass Function

The change of the abundance of haloes across different dark matter models is evident in Fig. 1, where dark matter density maps are shown for the CDM, the $m_{22} = 2$ and the $m_{22} = 0.25$ models, respectively. We quantify the abundance of FDM (and CDM) haloes as a function of their virial mass as measured from our cosmological volume simulations. Fig. 2 shows the differential (left) and cumulative (right) HMF derived from our FDM volume simulations at $z = 0$ for seven FDM particle masses. We verified that the measured CDM HMF matches the theoretical scaling of $\propto M_{\text{vir}}^{-0.9}$ ([Springel et al. 2008b](#)), shown by the dashed black line. The HMF computed using the fitting formula given by [Schive et al. \(2016\)](#) is plotted in dash-dotted curves for each FDM particle mass. As can be seen from Fig. 2, the FDM HMFs match the CDM one on large scales, with the cut-off scale varying depending on the FDM mass. As expected, the suppression of structure is stronger the lower the particle mass (as $Q \propto 1/m_{\chi}^2$).

4.2 Subhalo Mass Function

We quantify the abundance of subhaloes using the cumulative SHMF, which represents the number of subhaloes that are found in a system above a given mass. To make full use of the large number of systems present in each volume simulation, we average the SHMFs across all systems falling within three specific virial mass bins. One bin – hereafter referred to as the MW-like bin – represents the range that includes the Milky-Way halo virial mass $10^{11.5} M_{\odot} \leq M_{\text{vir}} \leq 10^{12.5} M_{\odot}$. The other two mass bins – hereafter referred to as bin 3 and bin 1 – encompass the ranges above and below, respectively. For consistency in the intra-bin average among systems of different masses, we express the SHMF in terms of the satellite-to-virial mass ratio $\hat{m} \equiv m_{\text{sat}}/M_{\text{vir}}$ before averaging over the different systems.

Fig. 3 shows the SHMFs for CDM and FDM with different FDM particle masses for the three mass bins. The left plot represents systems within bin 1, the middle plot corresponds to systems within the MW-like bin, and the right plot is for systems within bin 3. For bin 3 (the highest mass bin), we observe a suppression at low \hat{m} , which indicates that these large systems suffer an increasing lack of the smallest satellites as the FDM mass decreases. Likewise, the MW-like (middle mass) bin exhibits a similar trend, with the impact

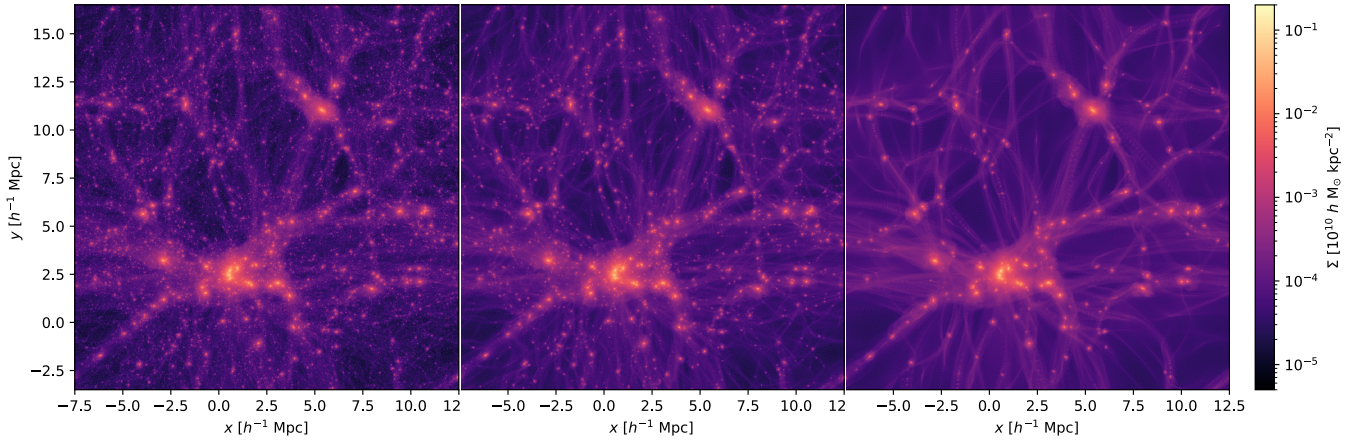


Figure 1. Dark matter density maps of the volume simulations. From left to right: CDM, FDM with $m_{22} = 2$ and FDM with $m_{22} = 0.25$.

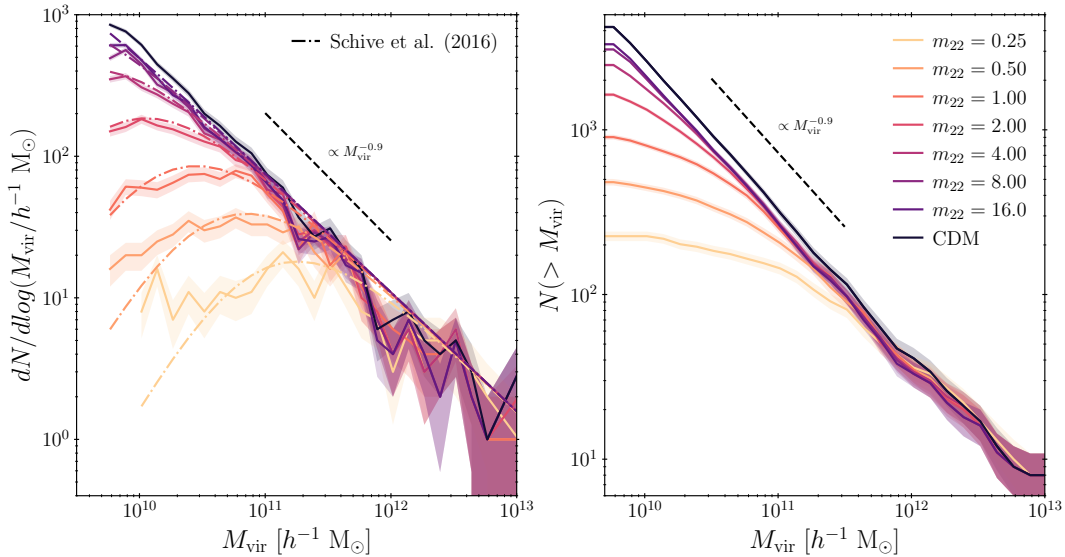


Figure 2. The CDM and FDM differential (left) and cumulative (right) HMF for different FDM masses. The dashed black line is the HMF scaling obtained in [Springel et al. \(2008b\)](#) for CDM. The HMF given by [Schive et al. \(2016\)](#) fitting formula are shown by the dash-dotted curves on the left plot. The 1σ statistical errors are shown as shaded regions.

of FDM extending to the largest satellites for the lowest FDM masses. Notably, bin 1 (the lowest mass bin) appears to show no significant deviation. This is because the suppression due to FDM is so strong that it impacts the mass scales of the host haloes, and hence those affected systems are completely absent. Similar to the pattern observed in the HMF, we find that the suppression of substructure is stronger for lower FDM masses.

For the MW-like bin, we provide a fitting formula for the FDM-to-CDM subhalo abundance ratio which takes the following analytical form:

$$\frac{\langle N(> \tilde{m})_{FDM} \rangle}{\langle N(> \tilde{m})_{CDM} \rangle} = \tanh(\kappa m_{22}^\beta) e^{\mu m_{22}^{-\gamma} \tilde{m}}, \quad (18)$$

where κ, β, μ and γ are free parameters which we fit using Markov Chain Monte Carlo (MCMC) technique utilizing the MCMC python package EMCEE ([Foreman-Mackey et al. 2013](#)). Using flat priors, we obtain the following mean poste-

rior values for the parameters $\kappa = 0.448$, $\beta = 0.817$, $\mu = 4.27$ and $\gamma = 0.434$ from the MCMC run. The left plot of Fig. 4 shows the FDM-to-CDM cumulative subhalo abundance ratio as obtained from the simulations (solid curves), as well as their respective fits (dashed curves) which were computed using Eq. 18.

To quantify the suppression of substructure abundance for different FDM masses with respect to CDM, we define the parameter α as:

$$\alpha \equiv \left. \frac{\langle N(> \tilde{m})_{FDM} \rangle}{\langle N(> \tilde{m})_{CDM} \rangle} \right|_{\tilde{m} \approx 10^{-3}}, \quad (19)$$

which represents the FDM-to-CDM ratio of the average number of subhaloes residing in MW-like systems and that have masses larger than $\approx 1/1000$ of their host virial mass. Thus, this new variable α captures the departure of FDM models from CDM in terms of substructure abundance suppression in MW-like systems (where by definition, $\alpha = 1$ for

a particular FDM model indicates that the FDM subhalo abundance identically matches that of CDM). To quantify the substructure suppression in FDM, the right plot of Fig. 4 shows α as a function of the FDM particle mass. The dashed black curve is the best-fit which was computed using Eq. 18 at $\tilde{m} \approx 10^{-3}$. For MW-like systems, this can be used to deduce that the satellite counts of $m_{22} \approx 0.1$ and $m_{22} \approx 1$ are 10% and 50% relative to CDM, respectively.

4.3 Properties of density cores

The radial density profiles of CDM and FDM subhaloes with particle masses $m_{22} \in \{8.00, 16.0, 32.0\}$ are measured from the zoom-in high-resolution simulations for systems A, B, C, and D, as presented in Fig. 5. The expected scalings for the NFW profile, characterized by a logarithmic inner slope of -1 representing the central cusp and a logarithmic outer slope of -3 representing the NFW envelope, are shown by the dashed and dotted black lines, respectively. As expected, the FDM subhaloes exhibit flat inner density profiles, indicating significant core formation, while the CDM subhaloes exhibit the expected central cusps.

From Fig. 5, it can be observed that significant cores are able to form in dwarf galaxies with mass of $\mathcal{O}(10^9 M_{\odot})$ in an FDM universe. This is important to emphasize since star formation has been shown to be insufficient to perturb the dark matter and induce the cusp-core transformation inside haloes with a mass below $5 \times 10^9 M_{\odot}$ (Di Cintio et al. 2014; Chan et al. 2015; Tollet et al. 2016), given the very limited contribution of stars and gas to the whole potential (e.g. Macciò et al. 2020).

To extract the FDM core radii from the radial profiles in Fig. 5, we employ the cored-NFW density profile formula given by Eq. 15. By imposing continuity at $r = r_t$, the number of free parameters are reduced by one to ρ_c, r_s, r_c, r_t . For each system, those four parameters are fitted by performing an MCMC exploration of the parameter space using the python package EMCEE (Foreman-Mackey et al. 2013).

For completeness, all the density profile parameter values r_c, ρ_c, r_s, r_t , and m_{22} for all four systems are given in Table 2. The density profile parameter values reported for each FDM mass are the median posterior distribution values from the MCMC run, while the mean parameter values are derived by averaging over all four systems. For the FDM masses $m_{22} \in \{8.00, 16.0, 32.0\}$, we find the mean core radii to be: $\langle r_c \rangle = 1.75 \pm 0.07 h^{-1}$ kpc, $\langle r_c \rangle = 0.88 \pm 0.04 h^{-1}$ kpc, and $\langle r_c \rangle = 0.45 \pm 0.02 h^{-1}$ kpc, respectively.

We investigate the dependence of the core properties given in Table 2 – namely the core radius and density – on the FDM particle mass. Fig. 6 presents the relations between r_c, ρ_c , and m_{22} for all four systems: $r_c \propto (m_{22}^2 \rho_c)^{-1/4}$, $r_c \propto m_{22}^{-1}$, and $\rho_c \propto m_{22}^2$. By extrapolating the core radius-FDM mass relation ($r_c \propto m_{22}^{-1}$) to lower masses, we are able to estimate the core radii for the FDM masses $m_{22} = \{0.25, 0.50, 1.00, 2.00, 4.00\}$ for systems which were not simulated in this work (as those specific systems were not present).

4.4 Catch-22 or not Catch-22

As a final step, we want to determine if there exists a *Catch-22* problem for FDM – namely, if there is a region in the parameter space where one can simultaneously have enough dark matter haloes to host the observed number of satellites around the MW and M31 while still form substantial cores in the dark matter distribution.

Given the inefficiency of star formation at low halo masses (e.g. Bullock et al. 2000; Behroozi et al. 2013; Buck et al. 2019), one needs to have a substantial population of dark matter haloes to act as possible cradles for the formation of dwarf satellite galaxies. In line with previous studies based on other dark matter models (Macciò & Fontanot 2010; Lovell et al. 2012; Lovell et al. 2014a), we exclude the region where $\alpha < 0.5$. This choice is quite arbitrary and mainly serves an illustrative purpose, demonstrating that substantial cores are formed even for more conservative FDM models. In fact, this is quite a conservative choice given that even models with a lower value of α might still be able to host the 30-40 satellites observed around our own galaxy. We plan to revisit this threshold once we have full hydrodynamical simulations in the FDM model. As will be discussed later, even though the constraint on α is only a rough one, Fig. 4 illustrates that the corresponding lower-limit on the FDM mass is quite insensitive to this α threshold.

On the density profiles side, we exclude $r_c > 2 h^{-1}$ kpc. Such large cores will be incompatible with current observations of the matter distribution in the most studied satellites on the MW, namely Carina, Fornax, Sextans and Sculptor (e.g. Read et al. 2019; Expósito-Márquez et al. 2023). From the $r_c - m_{22}$ relation shown in Fig. 6, excluding $r_c > 2 h^{-1}$ kpc corresponds to excluding $m_{22} \lesssim 8$.

Fig. 7 shows the $\alpha - r_c$ parameter space for the different FDM masses. The shaded regions correspond to the excluded regions in this parameter space (namely, $\alpha < 0.5$ and $r_c > 2 h^{-1}$ kpc). The core radii for the masses $m_{22} = \{0.25, 0.50, 1.00, 2.00, 4.00\}$ were estimated using the $r_c - m_{22}$ relation. The value of α for $m_{22} = 32$ was estimated using the fitting formula given by Eq. 18. The occupancy of the top-left unshaded region by FDM masses illustrates that it is possible to find a FDM particle mass interval – namely $m_{22} \gtrsim 8$ – where FDM produces both the observed substructure counts and core sizes at the same time. We therefore conclude that FDM does not undergo a *Catch-22* problem.

The simulations used in this work do not incorporate the effect of baryons on the dark matter. While baryonic physics is known to have non-trivial impact on the dark matter distribution on sub-galactic scale, it is important to stress that our conclusion that there is no *Catch-22* problem in FDM is expected to still hold even with the addition of baryons. This is illustrated by Fig. 7, where no matter how one shifts the α and/or r_c thresholds, there will *always* exist an unshaded region in the $\alpha - r_c$ parameter space that is occupied by FDM masses. In addition, the derived FDM mass constraint after the inclusion of baryons is not expected to be significantly different as well. This is the case because on the substructure abundance side, the FDM mass is quite insensitive to changes in α (refer to Fig. 4). This means that large changes in α translate to only marginal changes in the FDM mass constraint. Furthermore, as previously discussed

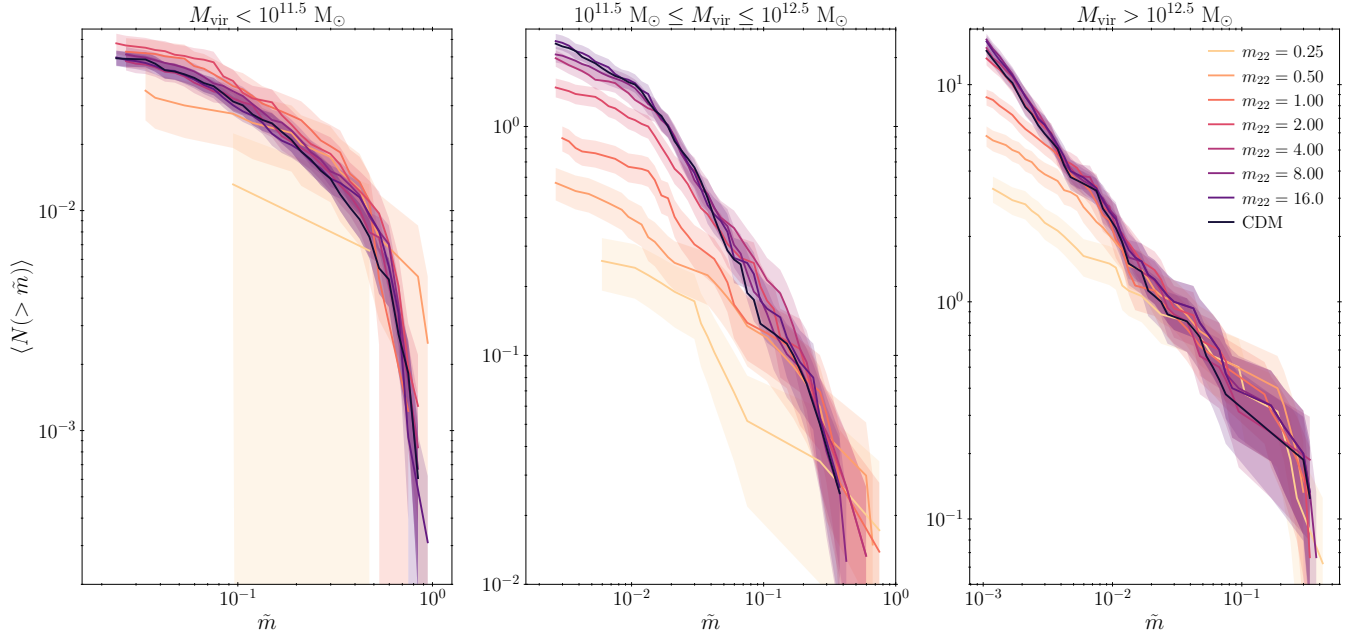


Figure 3. The cumulative SHMFs averaged over all systems with $M_{\text{vir}} < 10^{11.5} M_{\odot}$ (left plot), $10^{11.5} M_{\odot} < M_{\text{vir}} < 10^{12.5} M_{\odot}$ (middle plot), and $M_{\text{vir}} > 10^{12.5} M_{\odot}$ (right plot). The 1σ statistical errors are included as shaded regions.

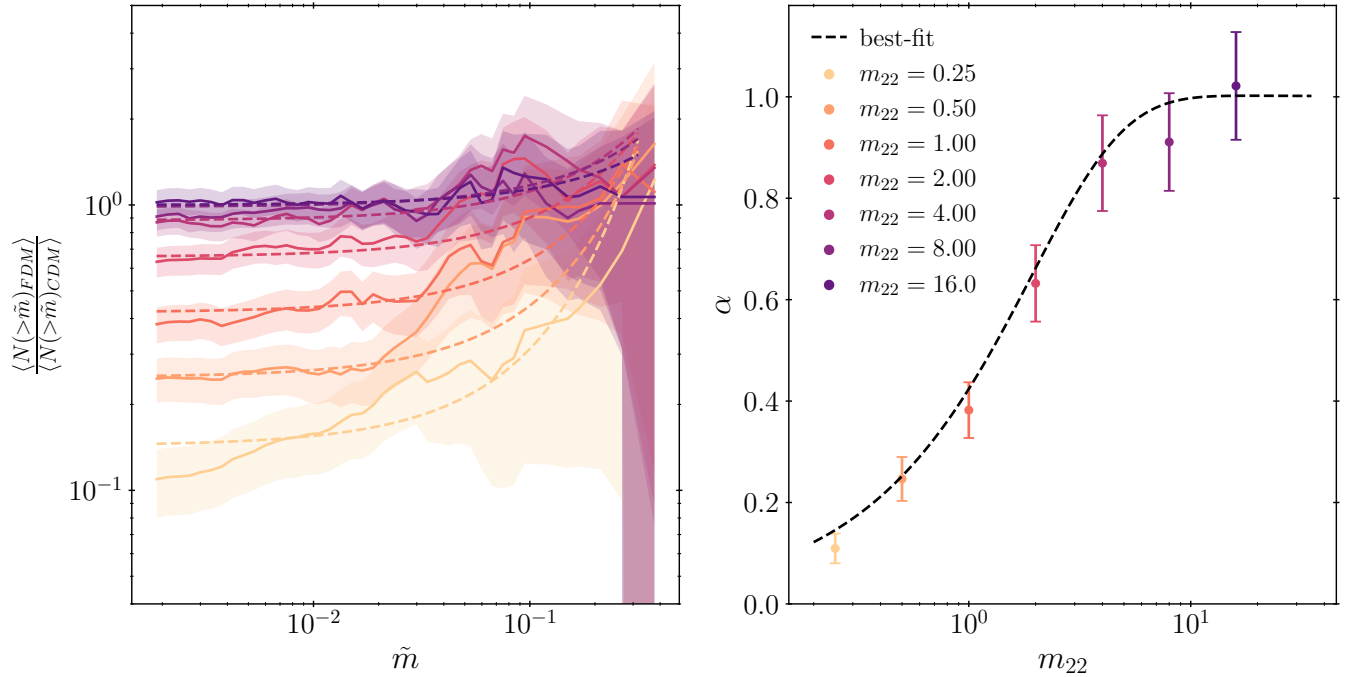


Figure 4. The left plot shows the FDM-to-CDM cumulative subhalo abundance ratio averaged over systems within the MW-like mass bin for different FDM masses. The dashed curves show this ratio computed using the fitting formula provided in this work which is given by Eq. 18. The 1σ statistical errors are included as shaded regions. The right plot (which is a subset of the left plot) shows the averaged FDM-to-CDM cumulative subhalo abundance ratio computed at $\tilde{m} \approx 10^{-3}$ as a function of the FDM mass. The dashed black curve is again the best-fitting result using Eq. 18.

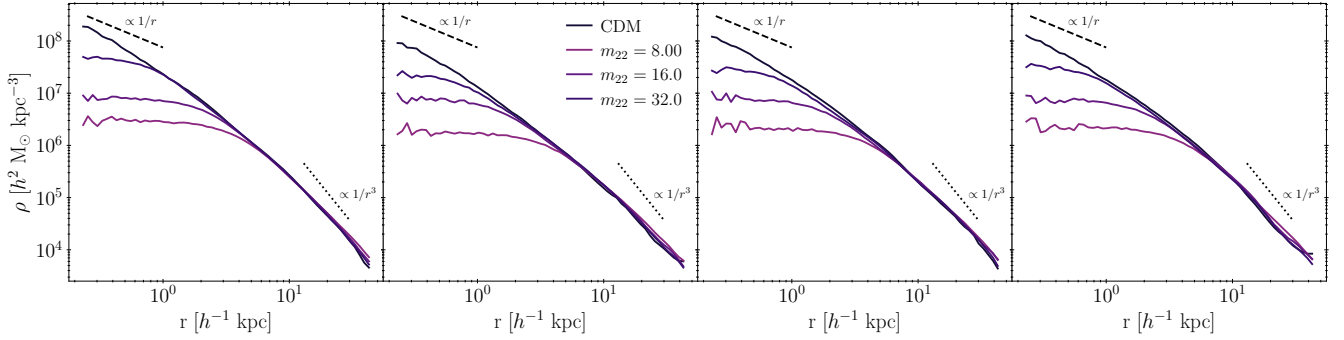


Figure 5. Radial density profiles for CDM and FDM with masses $m_{22} \in \{8.00, 16.0, 32.0\}$ for systems A, B, C, and D from left to right. The dashed and dotted black lines show the NFW profile scalings of $\propto r^{-1}$ and $\propto r^{-3}$, respectively.

m_{22}	System	r_c (h^{-1} kpc)	$\log(\rho_c/h^2 M_\odot \text{kpc}^{-3})$	r_s (h^{-1} kpc)	r_t (h^{-1} kpc)
8.00	A	1.66	7.16	2.88	1.98
	B	1.75	6.92	5.11	2.61
	C	1.77	7.02	3.36	2.07
	D	1.77	7.03	2.71	2.15
16.0	A	1.02	7.59	3.42	1.81
	B	0.807	7.54	3.34	1.18
	C	0.794	7.59	3.10	0.824
	D	0.895	7.57	2.56	0.976
32.0	A	0.466	8.29	2.38	0.843
	B	0.425	8.02	2.84	0.648
	C	0.456	8.11	2.29	0.639
	D	0.460	8.14	3.05	0.843
8.00		1.74	7.03	3.52	2.20
16.0	mean	0.880	7.57	3.10	1.20
32.0		0.451	8.14	2.64	0.744

Table 2. Density profile parameters for systems A, B, C, and D with particle masses $m_{22} \in \{8.00, 16.0, 32.0\}$, along with their mean values. The quoted parameter values are the median of the posterior distribution found from the MCMC run.

on the density profile front, the fact that we examined dwarf galaxies ($\approx 10^9 - 10^{10} M_\odot$) which are known to have only minimal baryonic content ensures that the core radii of such systems will not significantly change with the introduction of baryons.

5 CONCLUSIONS

We presented the FDM SubHalo Mass Function (SHMF) as measured from cosmological volume simulations which fully model the effects of the quantum potential throughout cosmic evolution for seven different FDM particle masses in the range $m_{22} \in [0.25 - 16]$. In addition, we computed the density profiles from zoom-in high-resolution simulations of dwarf galaxies for the FDM masses in the overlapping range $m_{22} \in [8 - 32]$, and used those to infer the size of the solitonic core within each dwarf galaxy. We summarize our main findings below:

- For the first time, we present a fitting functional form for the cumulative FDM-to-CDM SHMF ratio using FDM simulations that take full account of the dynamical effects of the quantum potential throughout cosmic evolution;
- In an FDM universe, we find that it is possible to form

significant cores in dwarf galaxies ($\approx 10^9 M_\odot$). This was reported to be very difficult to achieve with baryonic feedback alone;

- Unlike WDM, we conclude that FDM does not undergo a *Catch-22* problem. In particular, one can have particle masses ($m_{22} \gtrsim 8$) that simultaneously produce both substantial cores and the observed satellite abundances.

ACKNOWLEDGEMENTS

This material is based upon work supported by Tamkeen under the New York University Abu Dhabi Research Institute grant CASS. The authors gratefully acknowledge the High Performance Computing resources at New York University Abu Dhabi. MB is supported by the project ‘‘Combining Cosmic Microwave Background and Large Scale Structure data: an Integrated Approach for Addressing Fundamental Questions in Cosmology’’, funded by the MIUR Progetti di Ricerca di Rilevante Interesse Nazionale (PRIN) Bando 2017 - grant 2017YJYZAH.

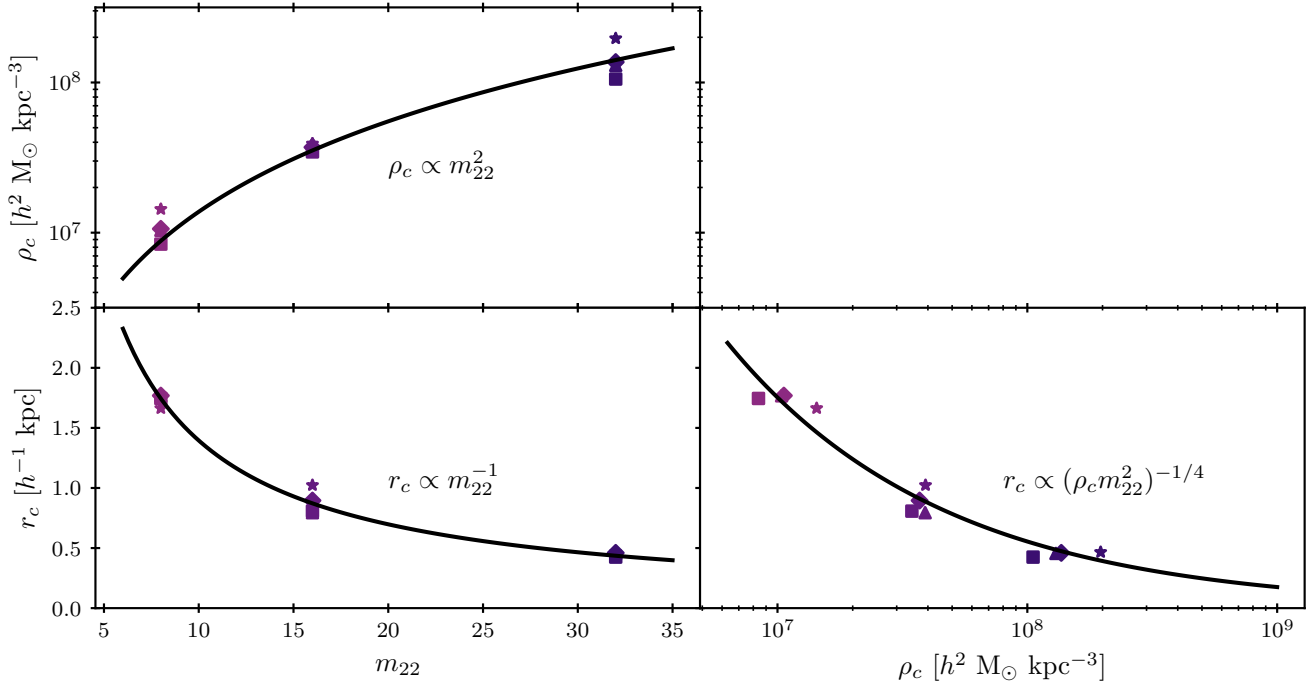


Figure 6. The FDM core-scaling relations. Upper and lower left plots show the core density and radius versus the FDM particle mass, respectively, while the lower right plot shows the core radius as a function of the core density. Systems A, B, C, and D are denoted by star, square, triangle, and diamond, respectively. The black curves show the respective best-fitting scaling relations.

DATA AVAILABILITY

The data underlying this article will be shared on reasonable request to the corresponding author.

References

- Abazajian K., 2006, *Physical Review D*, 73, 063506
Aghanim N., et al., 2020, *Astronomy & Astrophysics*, 641, A6
Alam S., et al., 2017, *MNRAS*, 470, 2617
Amendola L., Barbieri R., 2006, *Physics Letters B*, 642, 192
Amorisco N. C., Loeb A., 2018, arXiv preprint arXiv:1808.00464
Bahcall N. A., Lubin L. M., Dorman V., 1995, *The Astrophysical Journal*, 447, L81
Behroozi P. S., Wechsler R. H., Conroy C., 2013, *ApJ*, 770, 57
Bosma A., 1981, *The Astronomical Journal*, 86, 1825
Brooks A. M., Zolotov A., 2014, *The Astrophysical Journal*, 786, 87
Buck T., Macciò A. V., Dutton A. A., Obreja A., Frings J., 2019, *MNRAS*, 483, 1314
Bullock J. S., Kravtsov A. V., Weinberg D. H., 2000, *ApJ*, 539, 517
Chan T., Kereš D., Oñorbe J., Hopkins P., Muratov A., Faucher-Giguere C.-A., Quataert E., 2015, *Monthly Notices of the Royal Astronomical Society*, 454, 2981
Chan H. Y. J., Ferreira E. G., May S., Hayashi K., Chiba M., 2022, *Monthly Notices of the Royal Astronomical Society*, 511, 943
Chavanis P.-H., 2011, *Phys. Rev. D*, 84, 043531
Child H. L., Habib S., Heitmann K., Frontiere N., Finkel H., Pope A., Morozov V., 2018, *The Astrophysical Journal*, 859, 55
Copi C. J., Schramm D. N., Turner M. S., 1995, *Science*, 267, 192
Davis M., Efstathiou G., Frenk C. S., White S. D., 1985, *Astrophys. J.*, 292, 371
Di Cintio A., Brook C. B., Dutton A. A., Macciò A. V., Stinson G. S., Knebe A., 2014, *Monthly Notices of the Royal Astronomical Society*, 441, 2986
Dutton A. A., Macciò A. V., 2014, *MNRAS*, 441, 3359
Expósito-Márquez J., Brook C. B., Huertas-Company M., Di Cintio A., Macciò A. V., Grand R. J. J., Battaglia G., Arjona-Gálvez E., 2023, *MNRAS*, 519, 4384
Ferreira E. G., 2021, *The Astronomy and Astrophysics Review*, 29, 1
Fitts A., et al., 2017, *MNRAS*, 471, 3547
Foreman-Mackey D., Hogg D. W., Lang D., Goodman J., 2013, *Publications of the Astronomical Society of the Pacific*, 125, 306
Frings J., Macciò A., Buck T., Penzo C., Dutton A., Blank M., Obreja A., 2017, *MNRAS*, 472, 3378
Gilman D., Du X., Benson A., Birrer S., Nierenberg A., Treu T., 2020b, *Monthly Notices of the Royal Astronomical Society: Letters*, 492, L12
Gilman D., Du X., Benson A., Birrer S., Nierenberg A., Treu T., 2020a, *MNRAS*, 492, L12
Hlozek R., Grin D., Marsh D. J. E., Ferreira P. G., 2015, *Phys. Rev.*, D91, 103512
Hu W., Barkana R., Gruzinov A., 2000, *Phys. Rev. Lett.*, 85, 1158
Hui L., 2021, *Annual Review of Astronomy and Astrophysics*, 59, 247
Hui L., Ostriker J. P., Tremaine S., Witten E., 2017a, *Phys. Rev. D*, 95, 043541
Hui L., Ostriker J. P., Tremaine S., Witten E., 2017b, *Phys. Rev.*, D95, 043541
Ji S. U., Sin S. J., 1994, *Phys. Rev.*, D50, 3655
Komatsu E., et al., 2011, *ApJS*, 192, 18
Kulkarni M., Ostriker J. P., 2022, *Monthly Notices of the Royal Astronomical Society*, 510, 1425
Lovell M. R., et al., 2012, *MNRAS*, 420, 2318

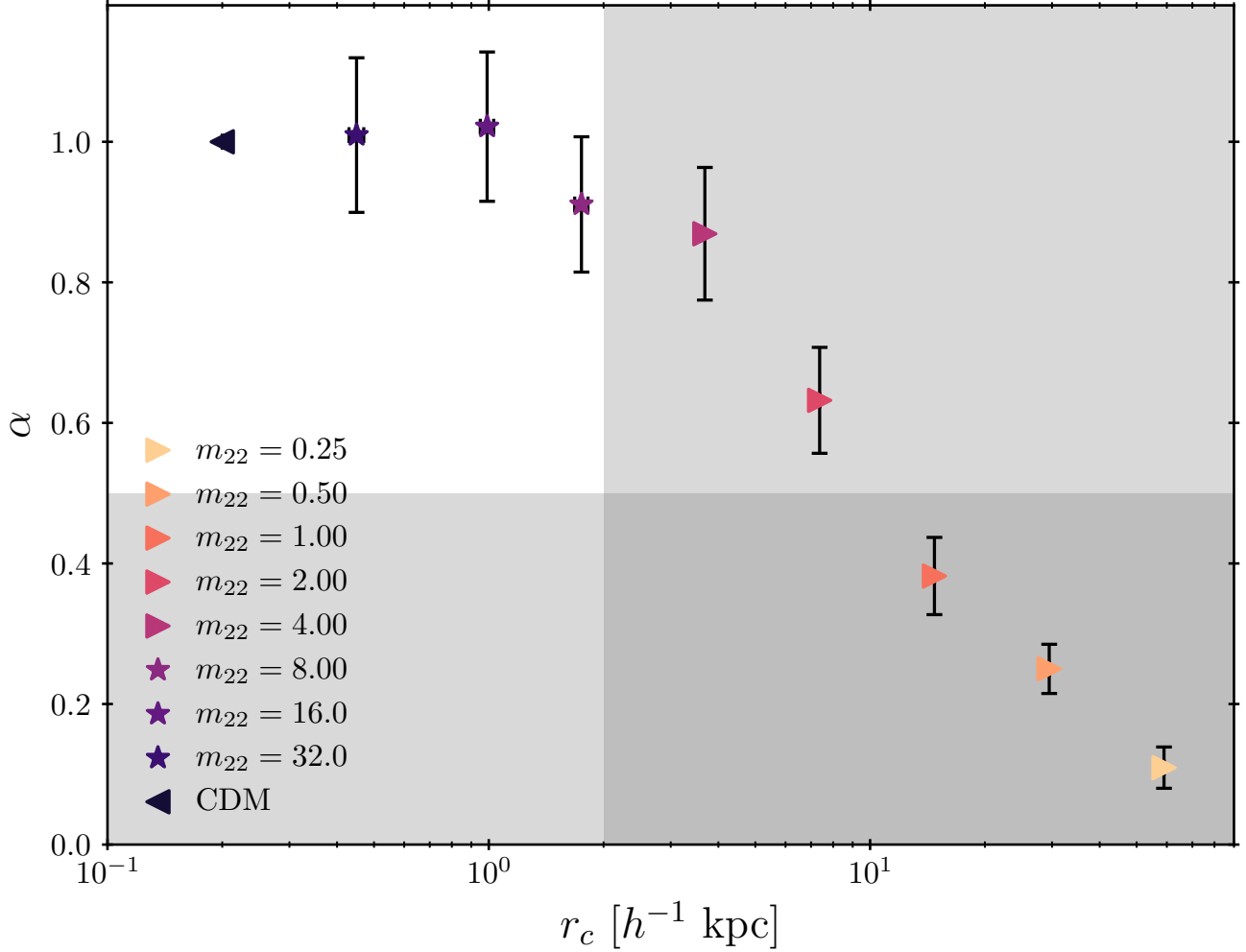


Figure 7. The FDM-to-CDM satellite abundance reduction ratio versus the core radius for all the FDM masses. The core radii for the masses $m_{22} \in \{0.25, 0.50, 1.00, 2.00, 4.00\}$ were found via extrapolation of the fitted core radius-mass scaling relation provided in Fig. 6. The grey regions corresponding to $\alpha < 0.5$ and $r_c > 2 h^{-1}$ kpc are the excluded regions. The occupancy of the top-left unshaded region by FDM masses illustrates the absence of a *Catch-22* problem in an FDM universe.

Lovell M. R., Frenk C. S., Eke V. R., Jenkins A., Gao L., Theuns T., 2014a, *Mon. Not. Roy. Astron. Soc.*, 439, 300
 Lovell M. R., Frenk C. S., Eke V. R., Jenkins A., Gao L., Theuns T., 2014b, *Monthly Notices of the Royal Astronomical Society*, 439, 300
 Ludlow A. D., Bose S., Angulo R. E., Wang L., Hellwing W. A., Navarro J. F., Cole S., Frenk C. S., 2016, *Monthly Notices of the Royal Astronomical Society*, 460, 1214
 Macciò A. V., Fontanot F., 2010, *Monthly Notices of the Royal Astronomical Society: Letters*, 404, L16
 Macciò A. V., Dutton A. A., van den Bosch F. C., Moore B., Potter D., Stadel J., 2007, *MNRAS*, 378, 55
 Macciò A. V., Paduroiu S., Anderhalden D., Schneider A., Moore B., 2012, *MNRAS*, 424, 1105
 Macciò A. V., Crespi S., Blank M., Kang X., 2020, *MNRAS*, 495, L46
 Madelung E., 1927, *Zeitschrift für Physik*, 40, 322
 Marsh D. J. E., 2016a, preprint, ([arXiv:1605.05973](https://arxiv.org/abs/1605.05973))
 Marsh D. J., 2016b, *Physics Reports*, 643, 1
 Navarro J. F., Eke V. R., Frenk C. S., 1996, *MNRAS*, 283, L72
 Navarro J. F., Frenk C. S., White S. D., 1997, *The Astrophysical*

Journal, 490, 493
 Nori M., Baldi M., 2018, *Mon. Not. Roy. Astron. Soc.*, 478, 3935
 Nori M., Murgia R., Iršič V., Baldi M., Viel M., 2019, *Mon. Not. Roy. Astron. Soc.*, 482, 3227
 Oñorbe J., Boylan-Kolchin M., Bullock J. S., Hopkins P. F., Kereš D., Faucher-Giguère C.-A., Quataert E., Murray N., 2015, *Monthly Notices of the Royal Astronomical Society*, 454, 2092
 Perlmutter S., et al., 1999, *ApJ*, 517, 565
 Planck Collaboration et al., 2016, *A&A*, 594, A13
 Read J. I., Walker M. G., Steger P., 2019, *MNRAS*, 484, 1401
 Riess A. G., et al., 1998, *AJ*, 116, 1009
 Rubin V. C., Ford W. K. J., Thonnard N., 1980, *ApJ*, 238, 471
 Schive H.-Y., Chiueh T., Broadhurst T., 2014a, *Nature Physics*, 10, 496
 Schive H.-Y., Liao M.-H., Woo T.-P., Wong S.-K., Chiueh T., Broadhurst T., Hwang W. P., 2014b, *Physical review letters*, 113, 261302
 Schive H.-Y., Chiueh T., Broadhurst T., Huang K.-W., 2016, *The Astrophysical Journal*, 818, 89
 Schneider A., Smith R. E., Macciò A. V., Moore B., 2012, *MNRAS*, 424, 684

- Springel V., et al., 2008a, *MNRAS*, **391**, 1685
 Springel V., et al., 2008b, Monthly Notices of the Royal Astronomical Society, **391**, 1685
 Tegmark M., et al., 2006, *Phys. Rev. D*, **74**, 123507
 Tollet E., et al., 2016, *MNRAS*, **456**, 3542
 Viel M., Lesgourgues J., Haehnelt M. G., Matarrese S., Riotto A., 2005, *Phys. Rev. D*, **71**, 063534
 Wang J., White S. D. M., 2007, *Mon. Not. Roy. Astron. Soc.*, **380**, 93
 Waterval S., et al., 2022, *MNRAS*, **514**, 5307
 Yang X., Mo H. J., van den Bosch F. C., 2003, *MNRAS*, **339**, 1057
 Zwicky F., 1937, *ApJ*, **86**, 217

APPENDIX A: CONCENTRATION-MASS RELATION

Instead of writing the NFW density profile given by Eq. 14 in terms of r_s and ρ_s , it can be written in terms of the dark matter halo mass and the halo concentration parameters. The halo concentration is defined by:

$$c_{\text{vir}} \equiv \frac{r_{\text{vir}}}{r_s}, \quad (\text{A1})$$

where r_{vir} is the virial radius. Eq. 14 then becomes:

$$\rho(r) = \frac{\rho_h}{3 \left[\ln(1 + c_{\text{vir}}) - \frac{c_{\text{vir}}}{1 + c_{\text{vir}}} \right] x \left(\frac{1}{c_{\text{vir}}} + x \right)^2}, \quad (\text{A2})$$

where $x \equiv r/r_{\text{vir}}$ is the fractional distance to the virial radius and $\rho_h \equiv \frac{3M_{\text{vir}}}{4\pi r_{\text{vir}}^3}$ is the average halo density within the virial radius.

The concentration-mass relation (hereafter $c(M)$) reflects the assembly history of haloes and is hence a powerful probe of models of structure formation (Gilman et al. 2020a). In standard CDM, the halo concentration has been shown to be a weakly decreasing function of halo mass (Dutton & Macciò 2014; Child et al. 2018; Gilman et al. 2020b). From the shape of the power spectrum of matter density perturbations (specifically that the variance increases at low masses), it follows that it is the small-scale perturbations that go nonlinear and undergo gravitational collapse earliest in the Universe, which gives rise to the current standard hierarchical picture of structure formation. The high concentration for low-mass haloes in CDM reflects the fact that those low-mass haloes formed at earlier times when the Universe had a higher background density (Navarro et al. 1997; Macciò et al. 2007).

We measure the halo concentrations in our CDM and FDM volume simulations of different particle masses, and excluding haloes containing less than 5000 particles. We also verify that, within statistical uncertainties, the expected $c(M)$ relation is obtained for CDM (Dutton & Macciò 2014). In contrast to CDM, we find that the FDM $c(M)$ relation is non-monotonic: while FDM halo concentrations follow the expected power-law relation as in CDM for high masses, we observe a drop in the FDM halo concentration for low halo masses. This decline in the halo concentration below a certain mass scale which is a function of the FDM mass is analogous to what has been observed in WDM (e.g. Schneider et al. 2012; Ludlow et al. 2016). The expected drop in halo concentration can be directly attributed to the delayed structure formation in FDM (and WDM) compared

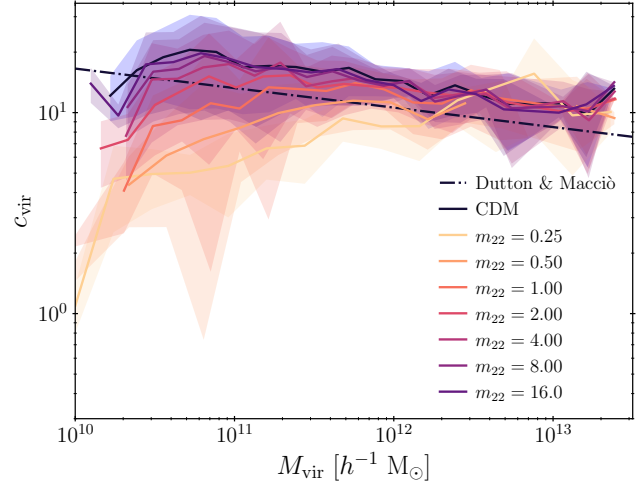


Figure A1. The concentration-mass relation for CDM and FDM with different particle masses. The expected power-law relation for CDM is shown in dash-dotted black (Dutton & Macciò 2014). The shaded regions show the 1σ Poissonian errors for each mass.

to CDM. This is because, as discussed before, the small-scale density perturbations below the quantum Jeans scale are stabilized by the quantum potential in FDM. Since the quantum Jeans scale is slowly shrinking with time (refer to Eq. 11), those small-scale perturbations do not collapse until a later time in the Universe when the Universe had a lower background density.